

Multifunctional nanocoated membranes for high-rate electrothermal desalination of hypersaline waters

Kuichang Zuo^{1,2,6}, Weipeng Wang^{2,3,6}, Akshay Deshmukh^{2,4}, Shuai Jia³, Hua Guo³, Ruikun Xin^{1,2}, Menachem Elimelech^{2,4}, Pulickel M. Ajayan^{2,3 ⋈}, Jun Lou^{2,3 ⋈} and Qilin Li^{1,2,3,5 ⋈}

Surface heating membrane distillation overcomes several limitations inherent in conventional membrane distillation technology. Here we report a successful effort to grow in situ a hexagonal boron nitride (hBN) nanocoating on a stainless-steel wire cloth (hBN-SSWC), and its application as a scalable electrothermal heating material in surface heating membrane distillation. The novel hBN-SSWC provides superior vapour permeability, thermal conductivity, electrical insulation and anticorrosion properties, all of which are critical for the long-term surface heating membrane distillation performance, particularly with hypersaline solutions. By simply attaching hBN-SSWC to a commercial membrane and providing power with an a.c. supply at household frequency, we demonstrate that hBN-SSWC is able to support an ultrahigh power intensity (50 kW m⁻²) to desalinate hypersaline solutions with exceptionally high water flux (and throughput), single-pass water recovery and heat utilization efficiency while maintaining excellent material stability. We also demonstrate the exceptional performance of hBN-SSWC in a scalable and compact spiral-wound electrothermal membrane distillation module.

our billion people around the world face at least one month of water scarcity every year¹, with 1.8 billion people living in countries experiencing absolute water scarcity². Desalination plays an important role in the utilization of alternative, saline water resources, in addition to protecting precious freshwater supplies from contamination by industrial wastewaters and brines. Reverse osmosis (RO) is at present the most widely used desalination technology due to its relatively low energy consumption3. However, the high pressure needed to overcome the osmotic pressure of hypersaline brines precludes its application in the desalination of key industrial waste streams, such as oil and gas produced water and RO concentrates as well as zero-liquid-discharge processes^{2,4}. Conventional thermal desalination methods, such as multi-effect distillation (MED) and multi-stage flash (MSF), are able to desalinate or concentrate brines beyond the salinity limit of RO5, but they require extensive infrastructure and high capital costs.

Membrane distillation (MD) is a hybrid thermal–membrane process. In MD, a hydrophobic, porous membrane separates the heated saline feed stream and the cool permeate stream. The temperature difference between the feed and permeate streams creates a gradient in the partial vapour pressure of the water vapour, driving its transport across the membrane⁶. After diffusing through the membrane, the water vapour condenses on the permeate side, producing pure water. The technology has the high salinity capability of conventional thermal desalination, enjoys the compact modular configuration of membrane systems, features low operating pressure and relatively low temperature, and it is also expected to be less prone to fouling than RO⁷. However, it suffers from several inherent limitations that result in very low thermal efficiencies (Supplementary

Section 1). Specifically, temperature polarization on both sides of the membrane reduces the vapour pressure difference and hence the flux; the average transmembrane temperature difference decreases with increasing feed channel length, resulting in decreasing average flux with increasing membrane module size; and limited heat capacity of the feed water relative to the high enthalpy of evaporation results in very low single-pass water recovery. In addition, heating the feed externally increases the system complexity and potential thermal energy loss.

Directly heating the feed stream at the membrane-solution interface has been proposed to address these limitations (Fig. 1a). Both solarthermal¹ and electrothermal⁸ coatings have been developed to achieve surface heating membrane distillation (SHMD). Solarthermal membranes utilize sunlight as the energy source, although water production rates are limited by its low energy intensity. Electrothermal MD utilizes spacer induction heating⁹ or Joule heating through an electrically conducting coating⁸, allowing the simple control of the energy input, although spacer heating heats the bulk feed water and is not considered to be SHMD. A recent study successfully demonstrated desalination using an MD membrane with an electrothermal coating consisting of multi-walled carbon nanotubes and polyvinyl alcohol (MWCNT/PVA)8. The MWCNT/ PVA coating, however, was susceptible to electrochemical corrosion in saline water, requiring high-frequency (10 kHz) a.c. power to protect it from degradation. Furthermore, its relatively low electrical conductivity together with its low electrochemical stability limit the surface energy input and hence the transmembrane water flux¹⁰. To be part of practical desalination technology, the electrothermal coating must possess the following: (1) high corrosion resistance,

¹Department of Civil and Environmental Engineering, Rice University, Houston, TX, USA. ²NSF Nanosystems Engineering Research Center Nanotechnology-Enabled Water Treatment (NEWT), Rice University, Houston, TX, USA. ³Department of Materials Science and NanoEngineering, Rice University, Houston, TX, USA. ⁴Department of Chemical and Environmental Engineering, Yale University, New Haven, CT, USA. ⁵Department of Chemical and Biomolecular Engineering, Rice University, Houston, TX, USA. ⁶These authors contributed equally: Kuichang Zuo, Weipeng Wang.

□ e-mail: ajayan@rice.edu; jlou@rice.edu; qilin.li@rice.edu

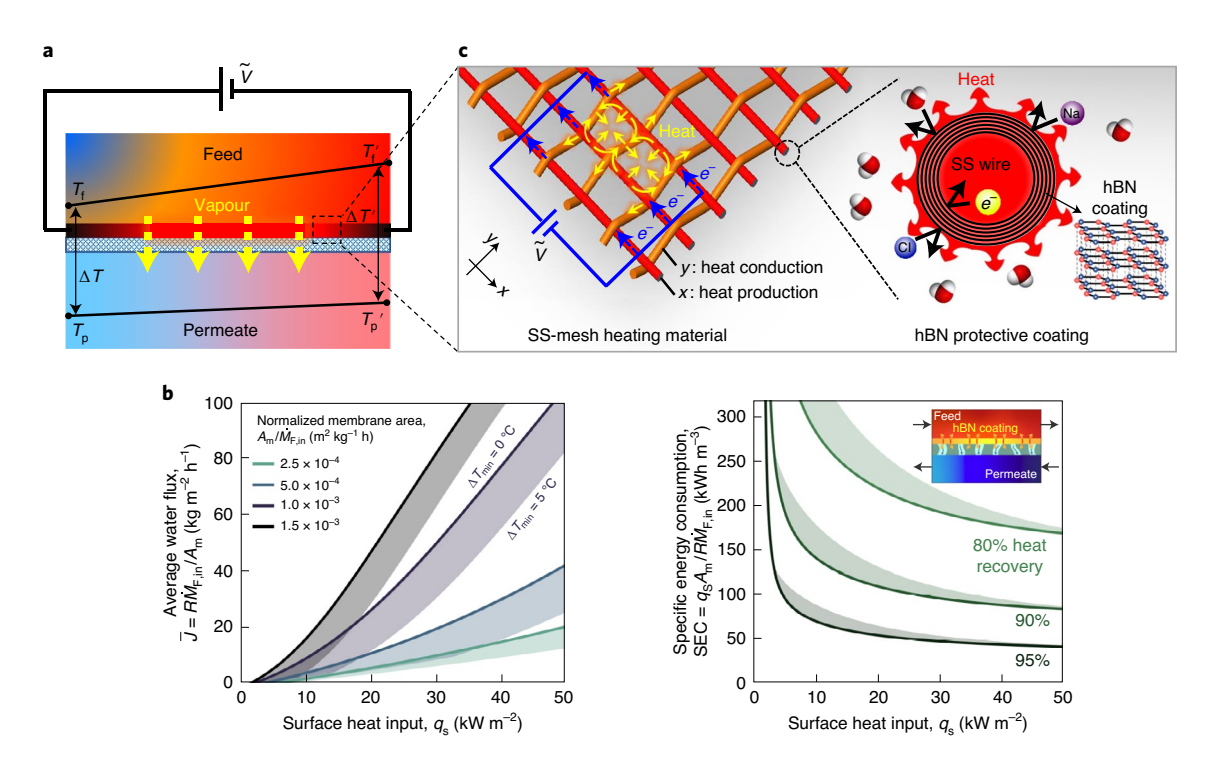


Fig. 1 | Hexagonal boron nitride as a multifunctional coating on SSWC in electrothermal SHMD. **a**, Direct surface heating at the membrane-brine interface maintains the transmembrane temperature gradient along the membrane length, and it reverses the temperature polarization on the feed side. T_{i} , T_{p} , T_{i}' , T_{p}' are the temperature of feed and permeate at the inlet and outlet of the SHMD reactor, respectively. \tilde{V} is the applied voltage. **b**, Left: finite-difference heat and mass transfer modelling demonstrates an extraordinary and sustained increase in the average water flux with surface heat input and normalized membrane area in an SHMD membrane module (Supplementary Section 3). R, water recovery ratio; $M_{F,in'}$ inlet mass flow rate of the feed stream; $A_{m'}$ membrane area. Shading represents the impact of increasing the minimum temperature difference in an external heat exchanger from 0 °C (solid curve, upper edge of each curve) to 5 °C (lower edge) for a given normalized membrane area. The feed salinity is 70 g kg⁻¹ and the membrane permeability coefficient is 5.0×10^{-6} kg m⁻² s⁻¹Pa⁻¹ (1,800 kg m⁻² h⁻¹bar⁻¹) throughout. Right: SEC as a function of the surface heat input for a single plate-and-frame SHMD membrane module (inset) with heat recovery efficiencies of 80%, 90% and 95% (Supplementary Section 3). The membrane permeability coefficient decreases from 4.0×10^{-6} kg m⁻² s⁻¹Pa⁻¹ (1,440 kg m⁻² h⁻¹bar⁻¹) at the lower edge of each curve to 1.0×10^{-6} kg m⁻² s⁻¹Pa⁻¹ (360 kg m⁻² h⁻¹bar⁻¹) at the lower edge of each curve to 1.0×10^{-6} kg m⁻² s⁻¹Pa⁻¹ (360 kg m⁻² h⁻¹bar⁻¹) at the lower edge of each curve to 1.0×10^{-6} kg m⁻² s⁻¹Pa⁻¹ (360 kg m⁻² h⁻¹bar⁻¹) at the lower edge of each curve to 1.0×10^{-6} kg m⁻² s⁻¹Pa⁻¹ (360 kg m⁻² h⁻¹bar⁻¹) at the lower edge of each curve to 1.0×10^{-6} kg m⁻² s⁻¹Pa⁻¹ (360 kg m⁻² h⁻¹bar⁻¹) at the lower edge of each curve to $1.0 \times 10^{-$

(2) high electrical conductivity (Supplementary Section 2), (3) high thermal conductivity, (4) superb electric insulation from the surrounding saline water and (5) high porosity. Our finite-difference modelling (Supplementary Section 3) illustrates the extraordinary increase in the average water flux (Fig. 1b, left) and decrease in the specific energy consumption (SEC) (Fig. 1b, right) with surface heat input, underscoring the importance of heating materials that can support high-energy operation.

Stainless-steel wire cloth (SSWC) is porous, flexible, robust and cheap, and it has microscopically uniform high thermal (12–45 W m⁻¹ K⁻¹) and electrical (bulk conductivity of 1.5×10⁶ S m⁻¹) conductivity. Although SSWC possesses outstanding anticorrosive performance in wet air and saline water, it faces the same challenge as the MWCNT/PVA coating when used in an electrothermal unit: electrochemical corrosion. One potential solution is to apply an insulating coating on the surface of the SSWC to prevent contact with saltwater and eliminate electrochemical corrosion (Fig. 1c). An effective coating would allow an SHMD system to be powered by low-frequency a.c. or even d.c. power sources.

Hexagonal boron nitride (hBN) is a van der Waals layered material, with a very similar lattice structure to graphene at the monolayer limit. It possesses many desirable properties including tunable thickness¹¹, ultraflat saturated surface¹², mechanical robustness¹³, large insulating bandgap and high dielectric constant¹⁴, excellent

thermal conductivity¹⁵, chemical stability against both strong acids and bases^{16,17} and high impermeability¹⁸. Consequently, hBN has been demonstrated to be a promising passivating coating for chemically active substrates in harsh environments¹⁹. More importantly, compared with other protective coating materials such as graphene, polymers and atomic-layer-deposited coatings^{20,21}, the electrically insulating yet highly thermally conducting properties of hBN combined with its impermeability to electrons, salt ions and gas and water molecules (Fig. 1c) are especially attractive as it provides a perfect chemical and electrical barrier while allowing rapid heat transfer. This is critical for the electrothermal heating of water as it eliminates Faradaic reactions such as water splitting on the heating element surface that may damage the membrane material, while maintaining efficient heat exchange. Although high-quality hBN nanofilm growth has been realized on nickel²², copper²³, iron²⁴ and their alloy substrates^{25,26}, growing high-quality hBN nanofilms on more commonly used metal substrates such as stainless steels has not been achieved, let alone the direct growth of hBN on porous SSWC considering its complex geometry.

Here we report the growth of high-quality hBN nanocoatings on SSWC surfaces (hBN-SSWC) and their application in electrothermal SHMD for the desalination of hypersaline waters. When laminated on a commercial PVDF (polyvinylidene difluoride) membrane, uniform Joule heating in the SSWC generated by a

ARTICLES

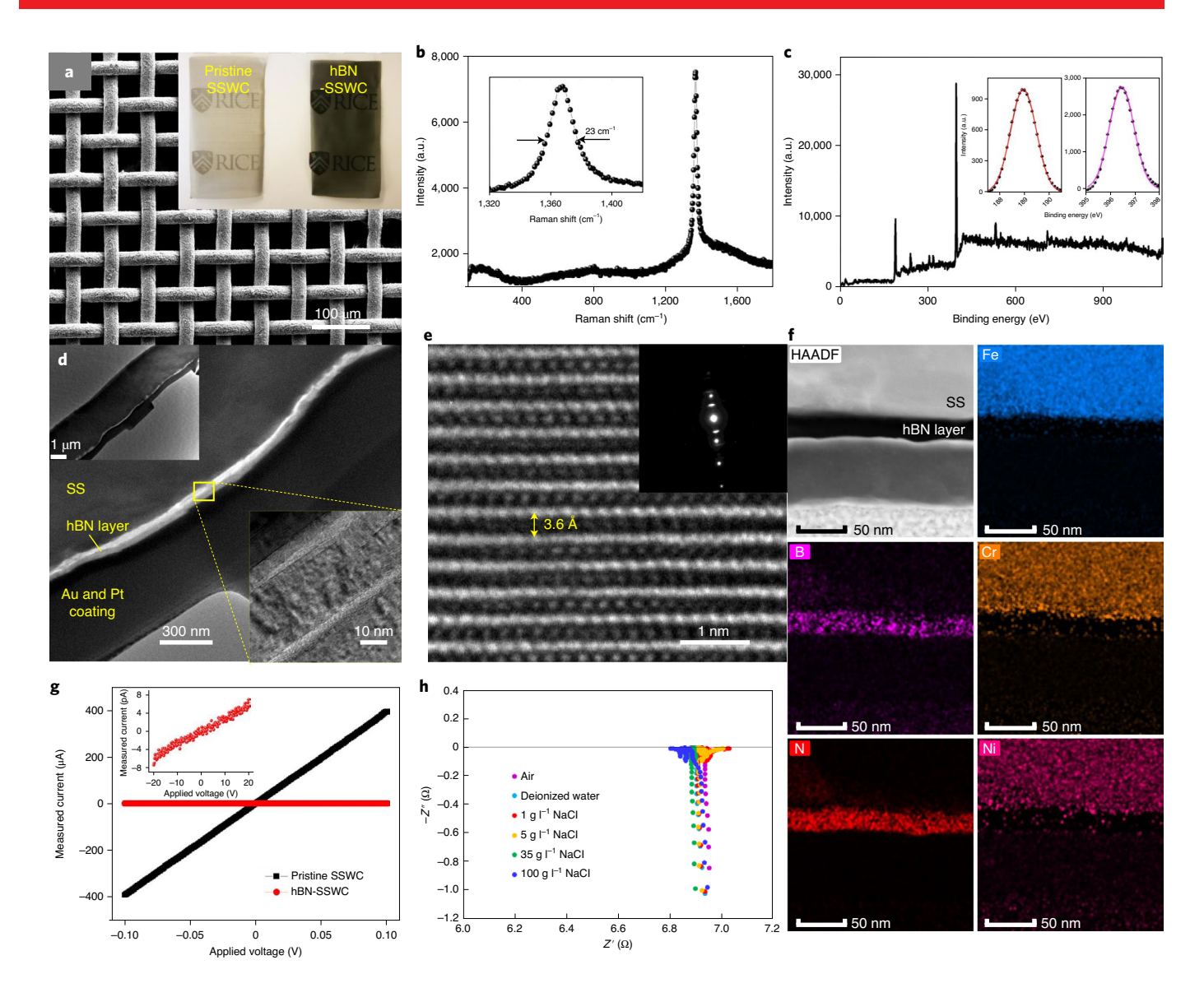


Fig. 2 | Growth of high-quality hBN nanocoatings on SSWC. a, SEM image of hBN-SSWC; the inset shows the photographs of pristine and hBN-coated SSWC. **b**, Raman spectrum of hBN-SSWC; the inset shows the FWHM. **c**, XPS spectrum of hBN-SSWC with fitted peaks of B1s (188.9 eV) and N1s (396.4 eV). The insets show the Gaussian fitted peaks of B1s (left) and N1s (right). **d**, Cross-sectional TEM images of hBN-SSWC at various magnifications. **e**, Atomic-resolution TEM of the hBN layers shows interlayer spacing of ~3.6 Å. The inset shows the selected area diffraction pattern. **f**, High-angle annular dark-field imaging (HAADF) and elemental maps of the sectional view of hBN-SSWC. **g**, The hBN nanocoating endows an excellent charge-insulating property in the cross direction, even under a test voltage between –20 and +20 V (inset). **h**, Electrochemical impedance spectroscopy data of hBN-SSWC at various salt concentrations. Z' and –Z" represent the real and imaginary part of the impedance, respectively.

voltage at household frequency (50 Hz) transfers efficiently to the saline feed water through the hBN coating (Fig. 1), leading to the rapid evaporation of water on the membrane surface and producing very high vapour fluxes. The exceptional electrical insulation and physical protection provided by the hBN nanocoating prevents chemical and electrochemical corrosion and any other undesirable reactions, ensuring long-term, stable performance of the SHMD in the desalination of hypersaline waters.

Growth of high-quality hBN on SSWC

The Fe and Ni elements in SSWC (ASTM 316) (Supplementary Fig. 7) are essential for direct hBN growth (Supplementary Section 4). The hBN nanocoating was directly grown using a conventional low-pressure chemical vapour deposition method on a 400-mesh-number SSWC (Fig. 2a). After hBN growth, the SSWC

turned dark brown and maintained its porous structure and excellent flexibility. The Raman spectrum (Fig. 2b) shows a strong, narrow peak located at 1,366 cm⁻¹ with full-width at half-maximum (FWHM) of 23 cm⁻¹, indicating the very high crystallinity of hBN. The X-ray photoemission spectroscopy (XPS) spectrum (Fig. 2c) reveals prominent N1s and B1s peaks, both well fitted using single Gaussian distribution with the peak centres located at 396.4 and 188.9 eV, respectively. These peaks as well as the stoichiometric atomic ratio (B:N=50:50) suggest that the hBN coating was of high quality without any elemental doping (for example, carbon atoms from the stainless-steel (SS) matrix). Cross-sectional transmission electron microscopy (TEM) images (Fig. 2d) confirm the layered structure of the as-grown hBN with a thickness of 80–100 nm over the observed area. Sufficient coating thickness is necessary to avoid 'weak points' caused by potential defects in each hBN layer,

particularly in large areas. The selected area diffraction pattern with extended, bright diffraction dots confirms the well-aligned layered structure. Atomic-resolution TEM (Fig. 2e and Supplementary Fig. 8) reveals a layered structure of hBN with interlayer spacing of ~3.6 Å and lattice constant of ~2.3 Å. As the hBN is directly grown on a curved surface of SS fibres, the cross-sectional TEM represents bent hBN layers. Energy-dispersive spectroscopy mapping (Fig. 2f) shows the uniform distribution of B and N elements throughout the hBN layer and a clear interface between the hBN layer and SS matrix. It is noteworthy that N and B are also observed on the top surface of the SS matrix, indicating a possible diffusion–nucleation growth mechanism²⁷.

The direct growth of high-quality hBN layers on SSWC enables outstanding insulation and anticorrosion performance in a unique environment in electrothermal SHMD. The electrical conductivity across the hBN nanocoating was characterized using an applied d.c. voltage (Fig. 2g). It shows resistance greater than $3 \times 10^{12} \Omega$ over an applied d.c. voltage between -20 and 20 V (inset of Fig. 2g), allowing high-power-input applications of hBN-coated SSWC. The ultrahigh electrical resistance, chemical inertness and impermeability of the hBN coating provide a complete barrier to mass (for example, salt ions and water molecules) and charge exchange between the saline water and SSWC, preventing any potential chemical and electrochemical reactions (Fig. 1c). This is demonstrated by the electrochemical impedance spectroscopy data, showing that the impedance of hBN-SSWC remained unchanged under the solution conditions over a wide range of salt concentrations (Fig. 2h) and pH values (Supplementary Fig. 9), while the pristine SSWC shows a dramatic impedance change when tested in high-salinity water (Supplementary Fig. 9). In addition, the hBN nanocoating efficiently conducts heat from the SSWC to the surrounding environment: the coated SSWC could support intensive power input (as high as 100 kW m⁻²; Supplementary Fig. 10) and produce temperatures higher than 200 °C.

SHMD enabled by hBN-SSWC Joule heating

The high-quality hBN nanocoating (Fig. 2a-f) and its protective barrier function (Fig. 2g,h) suggest that hBN-SSWC could be used for high-efficiency electrothermal SHMD. By attaching the pristine or hBN-coated SSWC on top of a PVDF membrane in the feed chamber of a custom-built SHMD cell, we desalinated hypersaline water (100 gl⁻¹ NaCl) under the single-pass operation mode at various input power densities (1-50 kW m⁻²) (Fig. 3a and Supplementary Section 5). Current production (Fig. 3b), membrane flux (Fig. 3c), effluent salt concentration (Fig. 3d) and temperature of the influent and effluent of the feed and permeate (Supplementary Fig. 11) were monitored. While consistently maintaining salt rejection of >99.9%, the membrane flux increased nonlinearly from 0.32 ± 0.03 to 42.7 ± 0.8 kg m⁻²h⁻¹ when the input power density increased from 1 to $50 \,\mathrm{kW}\,\mathrm{m}^{-2}$. The flux of $42.7 \pm 0.8 \,\mathrm{kg}\,\mathrm{m}^{-2}\,\mathrm{h}^{-1}$ in the hBN-SSWC SHMD is five times as high as that generated by the MWCNT/PVA coating (~8.5 kg m⁻² h⁻¹ (ref. 8)), and almost an order of magnitude higher than that generated by photothermal SHMD membranes $(0.5 \text{ kg m}^{-2} \text{h}^{-1} (\text{ref.}^{-1}))$. As the base membranes used in these studies have similar permeability, the large difference in membrane flux can be attributed to the difference in the energy input intensity achieved, which are 50.0, 11.1 and ~1.0 kW m⁻² for the hBN-SSWC, MWCNT/PVA and photothermal SHMD membranes, respectively. In conventional MD, the flux can be $>30 \text{ kg m}^{-2} \text{h}^{-1}$ with a cross-membrane temperature difference (ΔT) of 30–50 °C. However, ΔT decreases with the membrane length; achieving a high temperature difference in large membrane modules is a major challenge in process scale up28. In our approach, heat is produced on the membrane surface. The temperature of the feed stream, ΔT , and hence the local membrane flux increase with the membrane module length (Fig. 1a,b). The average membrane flux of the module, therefore, increases with the increasing module length 1 . At $50\,kW\,m^{-2}$, the high membrane flux resulted in highly concentrated brine $(302.9\,g\,l^{-1})$, corresponding to 67.0% single-pass water recovery. It is important to note that single-pass water recovery in conventional MD is limited to 6.4% (ref. 29) due to the decreasing feed temperature explained above. In the hBN-SSWC SHMD system, both membrane flux and single-pass water recovery can be further increased by increasing the membrane module length or reducing the feed-flow rate (that is, increasing the hydraulic retention time in the module). This is contrary to the case with conventional MD, which requires higher feed-flow rates to minimize the temperature polarization and supply the thermal energy for evaporation.

An important performance metric in MD is energy efficiency, which usually depends on the heat utilization efficiency (HUE; equation (2)) of the MD reactor itself, and the recovery and reuse of heat from the brine and the latent heat in the permeate vapour, the latter usually achieved by recirculating the brine and recovering the latent heat using an external heat exchanger29. Conventional MD suffers from very low single-pass HUE (HUE_{sp}) (0.76–8.09% (refs. 30-33)) due to its inherent limitations. Carefully designed heat recovery strategies can greatly improve the overall HUEsD to above 50-80% (refs. 9,34-36). The same strategies can also be used in SHMD systems to improve the energy efficiency. Previously reported SHMD studies, either photothermal or electrothermal, achieved much higher HUE_{sp}, but the flux was limited (Fig. 3f and Supplementary Section 7) under low-input-energy intensity. As shown in Figs. 1b and 3c, the membrane flux increases nonlinearly with the energy intensity because the water vapour pressure increases exponentially with the temperature as described by the Antoine equation^{37,38}. Higher flux directs more energy towards evaporation versus heating the feed stream, resulting in an increase in HUEsp with the energy input (Supplementary Table 2). The high electrical conductivity and excellent protective properties of hBN-SSWC enabled high-energy input (50 kW m $^{-2}$), thereby realizing HUE $_{sp}$ and flux values (56.8% and 42.7 kg m⁻²h⁻¹, respectively; Fig. 3e,f) that are much higher than those for either conventional MD or previously reported SHMD. It should be noted that the measured HUE_{sp} is a function of the membrane size and would be higher with better thermal insulation of the experimental system.

It is worth noting that the hBN nanocoating is critical for achieving the observed high performance. As a comparison, the pristine SSWC experienced severe disruption in performance when the input power density increased to 30 kW m⁻², as reflected by the current (Fig. 3b), flux (Fig. 3c) and feed-effluent temperature data (Supplementary Fig. 12a). It stopped working at 40 kW m⁻² due to corrosion-damage-induced breakdown. The scanning electron microscopy (SEM) images taken after the MD experiments confirmed that severe corrosion occurred on the pristine SSWC, while hBN-SSWC remained intact due to protection provided by the hBN nanocoating (Supplementary Fig. 13). A careful examination of the underlying PVDF membrane showed no damage on its porous structure after operation at 50 kW m⁻² (Supplementary Fig. 14). The liquid entry pressure also remained unchanged before $(0.325 \pm 0.015 \,\text{MPa} \,(\pm \text{s.d.}) \,\text{for PVDF})$ and after $(0.323 \pm 0.007 \,\text{MPa})$ (±s.d) for the hBN-SSWC-coated PVDF) operation. These results suggest that the high heating intensity of hBN-SSWC did not cause any deterioration of the PVDF membrane.

Stability of hBN-SSWC in SHMD operation

The long-term stability of hBN-SSWC was evaluated by operating the SHMD system at a constant power input density of $40\,\mathrm{kW}\,\mathrm{m}^{-2}$ and varying feed-flow rates (1, 0.5 and 0.17 ml min $^{-1}$) for 100 h. The performance was very stable under all the operating conditions in terms of flux (Fig. 4a), feed recovery and permeate quality (salt concentration ~5 mg l $^{-1}$). The current production also stabilized at

ARTICLES

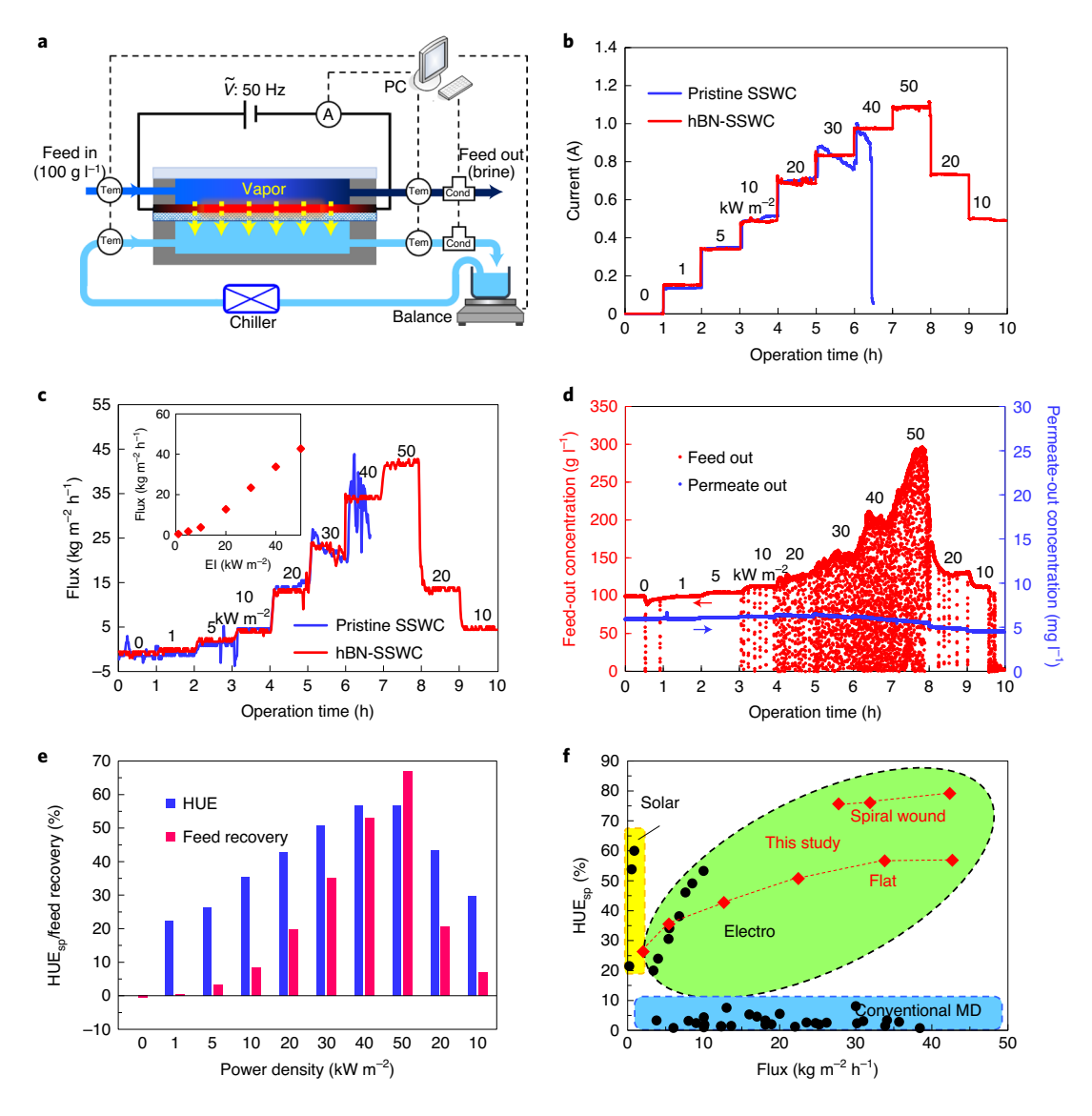


Fig. 3 | The hBN-SSWC supports high-energy input in SHMD to realize high performance. a, Schematic of the electrothermal SHMD experimental system. Tem, temperature sensor; Cond, conductivity sensor; PC, personal computer; $\hat{\mathbf{V}}$, applied voltage. **b**, Current production by pristine SSWC and hBN-coated SSWC. **c**, Membrane flux at various power densities; inset shows the nonlinear relationship between flux and energy intensity (EI). **d**, Effluent salt concentration of the feed and permeate in hBN-SSWC SHMD. **e**, HUE_{sp} and feed recovery in hBN-SSWC SHMD. **f**, Comparison of flux and HUE_{sp} of hBN-SSWC SHMD with the literature data. Each data point represents one published study, except for the red data points with varying power densities reported in this study (Supplementary Table 5).

 0.89 ± 0.03 A at all the feed-flow rates, indicating negligible impact of the feed-flow rate or brine concentration (Fig. 4b). Raman mapping (Fig. 4c) and XPS characterization (Fig. 4d) of hBN-SSWC after the 100h experiment showed no detectable change in the hBN nanocoating. Further, hBN has been reported to withstand extreme conditions with temperature up to 800 °C (ref. 39), voltage up to $1.2 \times 10^7 \,\mathrm{V\,cm^{-1}}$ (ref. ⁴⁰) and a broad range of pH (2-14). In the electrothermal SHMD operation, although a high power density (40 kW m⁻²) was utilized, the temperature on the hBN-SSWC surface is <100 °C due to the presence of liquid water. The voltage gradient across the hBN nanocoating (~106 V cm⁻¹) was also much lower than its breakdown threshold. Because hBN is non-abrasive and has similar thermal expansivity to SS, it is also unlikely to crack when the temperature varies. The Tafel test further supports that hBN-SSWC showed negligible change before and after the SHMD experiment (Fig. 4e), indicating no degradation or damage of the hBN nanocoating.

Magnified hBN-SSWC in novel spiral-wound electrothermal SHMD

The flexibility and porous structure of SSWC facilitates the large-scale growth of the hBN coating in a common tube furnace. In our study, an hBN-SSWC sample of 2 cm×85 cm was prepared in a furnace with a tubing diameter of 4.6 cm (Fig. 5a). Raman study showed that a high-quality, ~50 nm hBN coating was uniformly grown over the whole surface of the large SSWC sample (Supplementary Fig. 15 and Supplementary Section 6). With the large hBN-SSWC sample, a novel spiral-wound SHMD module was constructed with the hBN-SSWC sandwiched between two flat-sheet PVDF membranes and rolled into a cylindrical housing (Supplementary Fig. 16). The feed stream flows in the channel formed between the two membrane sheets, while the cold permeate stream flows outside the 'sack' (Fig. 5b,c). Compared with the plate-and-frame configuration (Fig. 3a), the spiral-wound module has much higher membrane packing density (676 m² m³) and

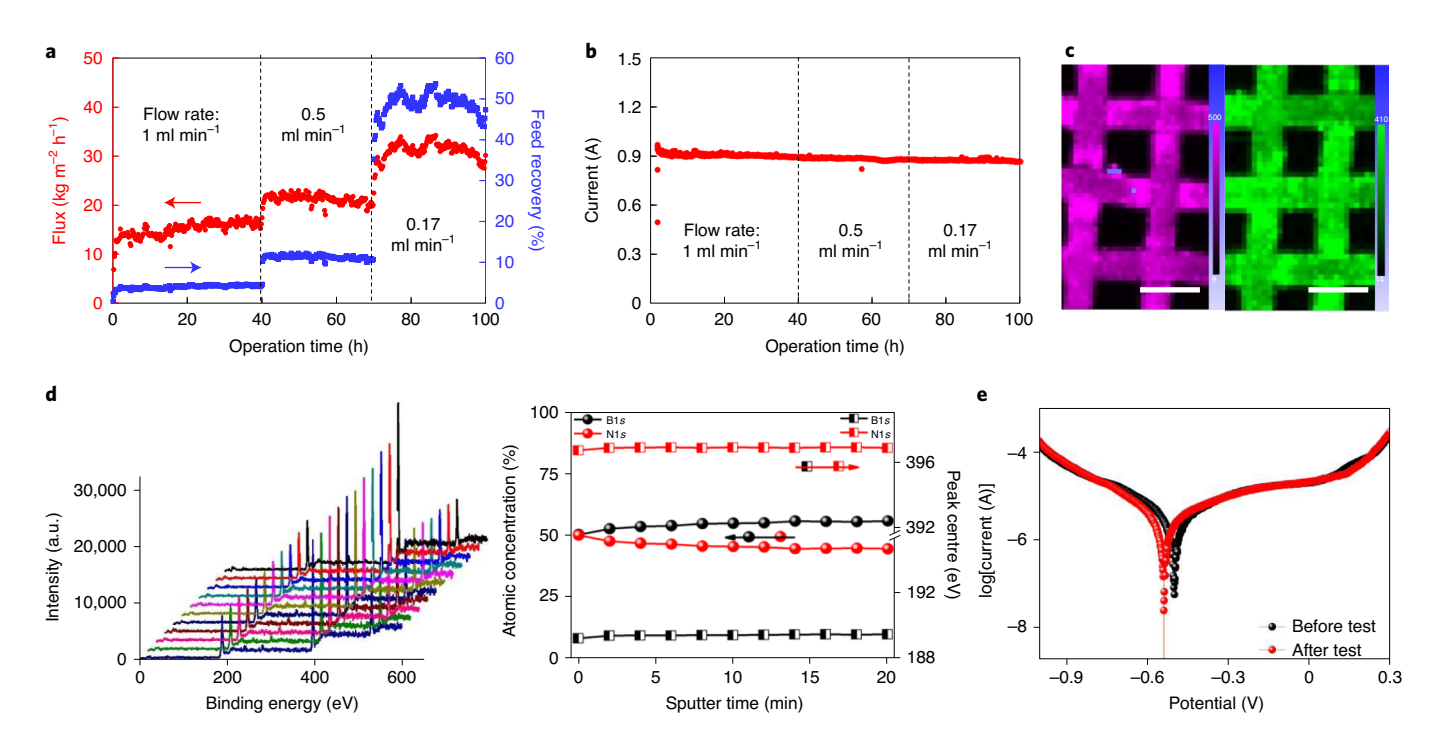


Fig. 4 | The hBN-coating-enabled long-term operation of SSWC in SHMD. a,b, Membrane flux, feed recovery (**a**) and current production (**b**) within 100 h operation under a power input of 40 kW m^{-2} . **c**, Raman intensity mapping at $1,366 \text{ cm}^{-1}$ before (left) and after (right) 100 h operation, revealing a cohesive, uniform coating. Scale bars, $50 \mu \text{m}$. The colour scale bars represent the Raman intensity of the $1,366 \text{ cm}^{-1}$ peak. **d**, XPS depth profile of hBN-SSWC after operation (left), and in-depth elemental ratio and B1s and N1s binding energies (right). **e**, Tafel curve of hBN-SSWC in $100 \text{ g} \text{ l}^{-1}$ NaCl solution before and after operation.

hence greatly reduces the system footprint for a given membrane area. More importantly, this design allows the hBN-SSWC coating to heat two membrane sheets at the same time and minimizes heat dissipation to the environment, greatly increasing the water production rate and reactor HUE_{sp}. With 36.5 kW m⁻² power input, the volumetric energy intensity reached 23.2 kW l⁻¹, producing flux of 42.4 kg m⁻² h⁻¹ (based on the hBN-SSWC area; Supplementary Table 4) when desalinating $100 \, \text{gl}^{-1}$ NaCl, which is 30.7% higher than that obtained using the plate-and-frame configuration at $40 \, \text{kW} \, \text{m}^{-2}$ (33.8 kg m⁻² h⁻¹). Similarly, the reactor HUE_{sp} increased from 56.8% (Fig. 3f) to 79.1% (Fig. 5d and Supplementary Table 4).

The high packing density and reactor HUE_{sp} of the spiral-wound module result in a very high throughput (volume of clean water produced per unit reactor volume per unit time) of $27.01l^{-1}$ h⁻¹ when desalinating a $100\,\mathrm{g}\,l^{-1}$ NaCl solution using a power input of $36.5\,\mathrm{kW}\,\mathrm{m}^{-2}$ (Fig. 5e). Together with its capability to treat feed streams of very high salt concentration (Supplementary Table 6 and Fig. 5e), it provides a compact, high-throughput solution for hypersaline water treatment, filling a critical technological gap in current thermal and RO-based desalination technologies. As shown in Fig. 5e and Supplementary Table 6, RO systems are highly compact with volumetric flux up to $26\,ll^{-1}\,h^{-1}$, but they are limited to $\sim\!80\,\mathrm{g}\,l^{-1}$ in feed-water salt concentration. Thermal desalination methods such as MSF, MED and mechanical vapour compression (MVC) can handle a wide range of salt concentrations, but they have very low throughput (usually $<\!11l^{-1}\,h^{-1}$) and hence the reactor size is very large.

Clearly, a desalination technology that can offer high membrane flux over a wide range of salt concentrations and low energy consumption is highly desirable. Intensive consumption of electricity—a higher-quality form of energy compared with heat—is the main concern in electricity-powered MD. In the spiral-wound SHMD, the higher HUE_{sp} (79.1%) realized an energy consumption of $875.8 \, \text{kWh m}^{-3}$ of clean water produced with no heat recovery.

Despite being one of the the lowest energy consumptions achieved in any MD processes without heat recovery, it is much higher than those of RO and other thermal technologies. Efficient heat recovery is critical to lower energy consumption for any MD systems. Incorporating effective heat recovery measures, such as brine recirculation and vapour heat exchange with raw feed water through multi-stage or multi-effect designs, have the potential to reduce the SEC to under 50 kWh m⁻³ (Fig. 1b). The heat input and membrane area per unit feed-flow rate of the hBN-SSWC SHMD system can be tailored to maximize the average water flux, reduce the areal footprint or minimize the SEC depending on the specific application. The spiral-wound hBN-SSWC SHMD would be a highly attractive solution to treat hypersaline waste streams, such as RO brine, oil and gas produced water and food-processing wastewater, as well as zero liquid discharge at high throughput, particularly where the system footprint is critical (such as offshore platforms). Other attractive features of the system include simplicity (for example, no need for external heater or feed recirculation loop), scalability (modular configuration with no restriction on module length) and the capability of operating using a household power source (50 Hz). When available, alternative energy sources including low-grade industrial waste heat, solarthermal energy and geothermal heating can be used to reduce the electrical energy consumption of hBN-SSWC SHMD, while electrothermal heating using hBN-SSWC ensures the high throughput and water recovery needed.

Several important issues need to be addressed in future research to facilitate the practical applications of hBN-SSWC SHMD technology. The long-term stability of the hBN coating in realistic feed waters is of the utmost importance. The layered structure of hBN minimizes the impact of defects on any given layer, and it can be optimized to avoid electrochemical 'weak points'. The high temperature on the membrane surface and the reversed temperature polarization suggest unique fouling and scaling behaviour in the

ARTICLES

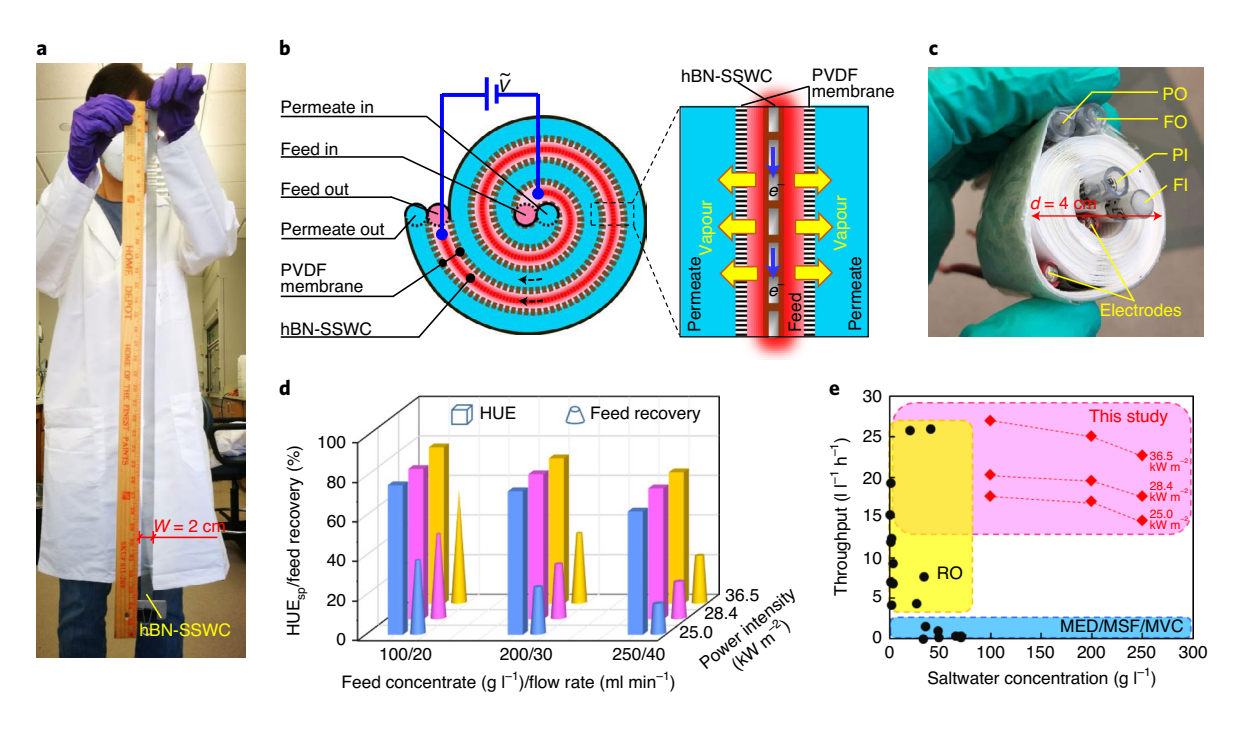


Fig. 5 | Magnified hBN-SSWC fabrication and its application in novel spiral-wound electrothermal SHMD. **a**, Synthesis of large hBN-SSWC with a length of 85 cm and a width (*W*) of 2 cm. **b**, Schematic of novel spiral-wound electrothermal SHMD. **c**, Photograph of the spiral-wound electrothermal SHMD during fabrication. FI, PI, FO, PO represent the inlet (I) and outlet (O) of the feed (F) and permeate (P). *d* is the diameter of the reactor. **d**, HUE_{sp} and feed recovery at various feed concentrations and power input intensities. **e**, Comparison of RO, MSF, MED, MVC and this study data in terms of throughput and feed-water salt concentration. Each data point represents one published study, except for the red data points with varying power densities reported in this study (Supplementary Table 6).

hBN-SSWC SHMD process: its investigation is important to avoid the deterioration of membrane performance due to wetting or decrease in vapour permeability. In addition, the scaling-up fabrication of the hBN coating at low cost is critical for its large-scale applications. The use of cheaper precursors and the automated and continuous feeding of SSWC rolls into the furnace are some of the potential ways to reduce the manufacturing cost. Finally, the efficient recovery of latent heat is critical for realizing low SECs (as shown in Fig. 1b), underscoring the importance of simple and low-cost multi-stage or multi-effect reactor designs.

The thin and porous structure, high resistance to corrosion and capability of generating high heat intensity of hBN-SSWCs may find broader applications in water and wastewater treatment as well as other industrial processes where the reaction kinetics limits the treatment efficiency. For example, it can be used as the support for catalysts in thermal–catalytic filters to enhance the catalytic reaction kinetics; it can also be used to deliver uniform, high heat intensity for the pyrolysis of refractory substances.

Conclusions

High-quality hBN nanocoating was successfully grown on SSWC, allowing it to function as an efficient and stable Joule heater in SHMD. The hBN coating serves as an excellent barrier to mass and charge exchange between hypersaline water and SSWC, while allowing efficient heat transfer. When combined with a commercial PVDF membrane in SHMD, hBN-SSWC enabled the high-performance desalination of hypersaline water with a power source of household frequency (50 Hz), simultaneously producing very high module-scale water flux, single-pass water recovery, reactor heat utilization efficiency and near-saturated brine. The hBN-SSWC also demonstrated excellent stability during long-term operation, with no observable (electro)chemical degradation or scraping of hBN-SSWC. The high flexibility and porosity of the SSWC enabled

the large-scale uniform growth of the hBN coating using existing chemical vapour deposition methods. The development of a novel yet simple spiral-wound SHMD module further improved the single-pass heat utilization efficiency and achieved very high reactor throughput, rendering it to be a highly attractive solution for hypersaline water treatment. The synergistic combination of material and system design in this study demonstrates how the unique properties of nanomaterials—when strategically integrated into a process—can be utilized to address highly challenging engineering problems and overcome the limitations of conventional technologies.

Online content

Any methods, additional references, Nature Research reporting summaries, source data, extended data, supplementary information, acknowledgements, peer review information; details of author contributions and competing interests; and statements of data and code availability are available at https://doi.org/10.1038/s41565-020-00777-0.

Received: 27 February 2019; Accepted: 9 September 2020; Published online: 26 October 2020

References

- Dongare, P. D. et al. Nanophotonics-enabled solar membrane distillation for off-grid water purification. Proc. Natl Acad. Sci. USA 114, 6936–6941 (2017).
- Deshmukh, A. et al. Membrane distillation at the water-energy nexus: limits, opportunities, and challenges. *Energy Environ. Sci.* 11, 1177–1196 (2018).
- Greenlee, L. F., Lawler, D. F., Freeman, B. D., Marrot, B. & Moulin, P. Reverse osmosis desalination: water sources, technology, and today's challenges. Water Res. 43, 2317–2348 (2009).
- 4. Elimelech, M. & Phillip, W. A. The future of seawater desalination: energy, technology, and the environment. *Science* 333, 712–717 (2011).
- Shaffer, D. L. et al. Desalination and reuse of high-salinity shale gas produced water: drivers, technologies, and future directions. *Environ. Sci. Technol.* 47, 9569–9583 (2013).

- Lawson, K. W. & Lloyd, D. R. Membrane distillation. J. Membr. Sci. 124, 1–25 (1997).
- Tow, E. W. et al. Comparison of fouling propensity between reverse osmosis, forward osmosis, and membrane distillation. *J. Membr. Sci.* 556, 352–364 (2018).
- 8. Dudchenko, A. V., Chen, C., Cardenas, A., Rolf, J. & Jassby, D. Frequency-dependent stability of CNT Joule heaters in ionizable media and desalination processes. *Nat. Nanotechnol.* **12**, 557–563 (2017).
- Tan, Y. Z., Chandrakant, S. P., Ang, J. S. T., Wang, H. & Chew, J. W. Localized induction heating of metallic spacers for energy-efficient membrane distillation. J. Membr. Sci. 606, 118150 (2020).
- Boo, C. & Elimelech, M. Thermal desalination membranes: carbon nanotubes keep up the heat. Nat. Nanotechnol. 12, 500–503 (2017).
- Song, L. et al. Large scale growth and characterization of atomic hexagonal boron nitride layers. Nano Lett. 10, 3209–3215 (2010).
- 12. Dean, C. R. et al. Boron nitride substrates for high-quality graphene electronics. *Nat. Nanotechnol.* **5**, 722–725 (2010).
- Falin, A. et al. Mechanical properties of atomically thin boron nitride and the role of interlayer interactions. *Nat. Commun.* 8, 15815 (2017).
- Watanabe, K., Taniguchi, T. & Kanda, H. Direct-bandgap properties and evidence for ultraviolet lasing of hexagonal boron nitride single crystal. *Nat. Mater.* 3, 404–409 (2004).
- 15. Jiang, P., Qian, X., Yang, R. & Lindsay, L. Anisotropic thermal transport in bulk hexagonal boron nitride. *Phys. Rev. Mater.* **2**, 064005 (2018).
- Chilkoor, G. et al. Hexagonal boron nitride: the thinnest insulating barrier to microbial corrosion. ACS Nano 12, 2242–2252 (2018).
- Zhang, J., Yang, Y. C. & Lou, J. Investigation of hexagonal boron nitride as an atomically thin corrosion passivation coating in aqueous solution. *Nanotechnology* 27, 364004 (2016).
- Hu, S. et al. Proton transport through one-atom-thick crystals. Nature 516, 227–230 (2014).
- Liu, Z. et al. Ultrathin high-temperature oxidation-resistant coatings of hexagonal boron nitride. Nat. Commun. 4, 2541 (2013).
- Costescu, R., Cahill, D., Fabreguette, F., Sechrist, Z. & George, S. Ultra-low thermal conductivity in W/Al₂O₃ nanolaminates. Science 303, 989–990 (2004).
- Abdulagatov, A. et al. Al₂O₃ and TiO₂ atomic layer deposition on copper for water corrosion resistance. ACS Appl. Mater. Interfaces 3, 4593–4601 (2011).
- Liu, Z. et al. In-plane heterostructures of graphene and hexagonal boron nitride with controlled domain sizes. Nat. Nanotechnol. 8, 119–124 (2013).
- Pakdel, A., Zhi, C., Bando, Y. & Golberg, D. Low-dimensional boron nitride nanomaterials. *Materials Today* 15, 256–265 (2012).
- Sun, J. et al. Recent progress in the tailored growth of two-dimensional hexagonal boron nitride via chemical vapour deposition. *Chem. Soc. Rev.* 47, 4242–4257 (2018).
- 25. Lu, G. et al. Synthesis of large single-crystal hexagonal boron nitride grains on Cu–Ni alloy. *Nat. Commun.* **6**, 6160 (2015).

- Lu, G. et al. Synthesis of high-quality graphene and hexagonal boron nitride monolayer in-plane heterostructure on Cu–Ni alloy. Adv. Sci. 4, 1700076 (2017).
- Zhang, Z., Liu, Y., Yang, Y. & Yakobson, B. I. Growth mechanism and morphology of hexagonal boron nitride. *Nano Lett.* 16, 1398–1403 (2016).
- Chen, T.-C., Ho, C.-D. & Yeh, H.-M. Theoretical modeling and experimental analysis of direct contact membrane distillation. *J. Membr. Sci.* 330, 279–287 (2009).
- Lin, S., Yip, N. Y. & Elimelech, M. Direct contact membrane distillation with heat recovery: thermodynamic insights from module scale modeling. *J. Membr. Sci.* 453, 498–515 (2014).
- Naidu, G., Jeong, S., Choi, Y. & Vigneswaran, S. Membrane distillation for wastewater reverse osmosis concentrate treatment with water reuse potential. J. Membr. Sci. 524, 565–575 (2017).
- Luo, W. H. et al. An osmotic membrane bioreactor–membrane distillation system for simultaneous wastewater reuse and seawater desalination: performance and implications. *Environ. Sci. Technol.* 51, 14311–14320 (2017).
- Efome, J. E., Rana, D., Matsuura, T. & Lan, C. Q. Enhanced performance of PVDF nanocomposite membrane by nanofiber coating: a membrane for sustainable desalination through MD. Water Res. 89, 39–49 (2016).
- Mericq, J. P., Laborie, S. & Cabassud, C. Vacuum membrane distillation of seawater reverse osmosis brines. Water Res. 44, 5260–5273 (2010).
- Zhang, Y., Peng, Y., Ji, S., Li, Z. & Chen, P. Review of thermal efficiency and heat recycling in membrane distillation processes. *Desalination* 367, 223–239 (2015).
- Leitch, M. E., Li, C., Ikkala, O., Mauter, M. S. & Lowry, G. V. Bacterial nanocellulose aerogel membranes: novel high-porosity materials for membrane distillation. *Environ. Sci. Technol. Lett.* 3, 85–91 (2016).
- Deshmukh, A. & Elimelech, M. Understanding the impact of membrane properties and transport phenomena on the energetic performance of membrane distillation desalination. *J. Membr. Sci.* 539, 458–474 (2017).
- Alsaadi, A. S. et al. Modeling of air-gap membrane distillation process: a theoretical and experimental study. J. Membr. Sci. 445, 53–65 (2013).
- Al-Obaidani, S. et al. Potential of membrane distillation in seawater desalination: thermal efficiency, sensitivity study and cost estimation. J. Membr. Sci. 323, 85–98 (2008).
- Tran, T. T., Bray, K., Ford, M. J., Toth, M. & Aharonovich, I. Quantum emission from hexagonal boron nitride monolayers. *Nat. Nanotechnol.* 11, 37–41 (2016).
- Hattori, Y., Taniguchi, T., Watanabe, K. & Nagashio, K. Layer-by-layer dielectric breakdown of hexagonal boron nitride. ACS Nano 9, 916–921 (2015).

Publisher's note Springer Nature remains neutral with regard to jurisdictional claims in published maps and institutional affiliations.

© The Author(s), under exclusive licence to Springer Nature Limited 2020

NATURE NANOTECHNOLOGY ARTICLES

Methods

Direct synthesis of hBN coating on SSWC. The synthesis of hBN was carried out in a quartz tube furnace. An SSWC with a mesh size of 400 (ASTM 316, McMaster-Carr) was washed with a diluted HNO $_3$ solution for 10 min and placed in the centre of the quartz tube furnace. A low pressure of 60 mtorr was maintained in the quartz tube during growth. The furnace temperature was raised to 1,050 °C in 45 min and maintained at 1,050 °C for 2 h under the protection of 50 s.c.c.m. hydrogen gas flow. Subsequently, ammonia borane (97%, Sigma-Aldrich) was introduced as the source of B and N and sublimated at 70 °C. The typical growth time was about 1–2 h. After growth, the sample was cooled to room temperature in the furnace.

Characterization of hBN-SSWC. Raman spectroscopy (Renishaw in Via) was performed at 532 nm laser excitation with power of 20 mW. The Raman mapping data were collected within an area of $100\,\mu\text{m}\times60\,\mu\text{m}$ with the spot resolution of $4\,\mu\text{m}\times4\,\mu\text{m}$. Field-emission SEM (FEI Quanta 400 ESEM FEG) was used to characterize the morphology of the pristine SSWC and hBN-coated SSWC before and after the MD experiments. XPS (PHI Quantera XPS) was performed using monochromatic Al Ka X-rays. Depth profiles were obtained with a 0.5 keV Ar^+ ion beam and alternative mode within an etching area of 3 mm \times 3 mm to etch the hBN-SSWC. For the as-grown hBN-SSWC, the TEM samples were prepared by a focused ion beam (FEI Helios SEM/FIB) with 30 keV Ga^+ ion gun. High-resolution TEM (FEI Titan Themis3) was operated at 300 keV to study the morphology of the hBN layers under the scanning TEM mode with double aberration correction. Electron energy loss spectra were collected using a Gatan's Enfina spectrometer with collection semi-angle of 48 mrad. The convergence semi-angle for the incident probe was 31 mrad, and the ADF images were collected for a half-angle range of \sim 54–200 mrad.

The Tafel curve was obtained in air at room temperature via a Desert probe station with Agilent B1500A semiconductor parameter analyser. Electric impedence spectra were collected by a CHI660 electrochemical station in air, diluted water and saline water from 35 to 100 gl $^{-1}$. The Tafel curves of pristine and post-test hBN-SSWC were obtained over a sample area of 5 cm \times 2 cm using a three-electrode arrangement with hBN-SSWC as the working electrode, Pt electrode as the counter electrode and Ag/AgCl electrode as the reference electrode.

SHMD reactors, operation and analysis. Flat SHMD fabrication and operation. The SHMD cell consists of two rectangular acrylic housing plates (Falken Design), two rubber gaskets and two plastic meshes (thickness, 1 mm; screen size, $\sim\!0.5$ mm $\times\!0.5$ mm), forming the flow channels of the feed and permeate separated by the PVDF membrane. The dimensions of the flow channel were 80 mm $\times\!2$ mm $\times\!1$ mm, providing an effective area of 1.6 cm². A pristine or hBN-coated SSWC was attached on the feed-side surface of the PVDF membrane, and it was utilized as the heating element. The hBN-SSWC or SSWC was connected to external wires at the two ends of the SHMD cell using conductive silver paint, where the connecting area was first polished using sand paper and then painted with epoxy resin to prevent corrosion.

In the experiments, the feed water contained $100\,\mathrm{g\,I^{-1}}$ NaCl, and it was pumped through the SHMD cell in a single pass at a flow rate of 0.17–1 ml min⁻¹ (cross-flow velocity of 17– $100\,\mathrm{cm\,min^{-1}}$), unless otherwise specified. Deionized water was used as the cooling stream and was circulated between an external reservoir, chiller and SHMD reactor at a flow rate of $8.5\,\mathrm{ml\,min^{-1}}$ and temperature of $20\,^{\circ}\mathrm{C}$. Further, a.c. ($50\,\mathrm{Hz}$) power densities of $0,\,1,\,5,\,10,\,20,\,30,\,40$ or $50\,\mathrm{kW\,m^{-2}}$ were applied to the heating element using a waveform generator and signal magnifier. The membrane flux was determined by monitoring the change in the cooling stream mass using an electric balance. The conductivity of the feed and permeate effluents was measured and recorded using conductivity sensors (ET908, eDAQ). The temperatures of the influent and effluent of both feed and permeate streams were monitored using temperature sensors. The current production

was measured with a multimeter (EX540, Extech). All the monitoring data were automatically recorded on a computer.

Calculation and analysis. In SHMD, the membrane flux $(J, \log m^{-2} h^{-1})$ is calculated to evaluate the water production rate:

$$J = \frac{\Delta M_{\rm p}}{\Delta t A_{\rm m}} \tag{1}$$

where $\Delta M_{\rm p}$ (kg) is the mass change in the cooling stream during a time period of Δt (h) and $A_{\rm m}$ (m²) is the effective membrane area.

 $\rm HUE_{sp}$ is defined as the percentage of input energy utilized to produce vapour in one pass of the feed solution through the reactor (that is, no heat recovery). It is fundamentally different from the thermal efficiency of conventional MD systems, which essentially means how much of the heat actually transferred is utilized for vapour transfer.

$$HUE_{sp} = \frac{J\rho_{w}^{-1}A_{m}\Delta H^{v}}{P_{in}} = \frac{J\rho_{w}^{-1}A_{m}\Delta H^{v}}{3.6UI}100\%$$
 (2)

Here, J is the membrane flux $(kg m^{-2} h^{-1})$, ρ_w is the density of the permeate $(kg l^{-1})$, A_m is the effective membrane area (m^2) , ΔH^v is the enthalpy of vaporization $(2,453 \, kJ \, l^{-1} \, at \, 20 \, ^{\circ} \text{C})$, U is the applied voltage (V), and I is the produced current (A). Here, P_{in} is the total electric power input intensity in this system $(kJ \, h^{-1})$. The numerator of this equation is the energy needed to produce vapour, while the denominator part represents the total power input.

Data availability

The datasets generated during and/or analysed during the current study are available from the corresponding author on reasonable request.

Code availability

The code utilized during the current study is available from the corresponding author on reasonable request.

Acknowledgements

This work was supported by the NSF Nanosystems Engineering Research Center for Nanotechnology-Enabled Water Treatment (EEC-1449500) and the NSF I/UCRC Center for Atomically Thin Multifunctional Coatings (ATOMIC) under award number IIP-1539999.

Author contributions

K.Z. and W.W. contributed equally to this work; they designed and performed the experiments, analysed the data and wrote the manuscript. J.L, Q.L., P.M.A. and M.E. conceived the idea, revised the manuscript and led the project. S.J., H.G., R.X. and A.D. assisted with the sample growth, TEM characterization, MD operation and simulation, respectively.

Competing interests

The authors declare no competing interests.

Additional information

Supplementary information is available for this paper at https://doi.org/10.1038/s41565-020-00777-0.

Correspondence and requests for materials should be addressed to P.M.A., J.L. or Q.L.

Peer review information Nature Nanotechnology thanks Shihong Lin and the other, anonymous, reviewer(s) for their contribution to the peer review of this work.

Reprints and permissions information is available at www.nature.com/reprints.